

# A Possible Correlation between the Gaseous Drag Strength and Resonant Planetesimals in Planetary Systems

Ing-Guey Jiang<sup>1</sup> and Li-Chin Yeh<sup>2</sup>

<sup>1</sup> Department of Physics,

National Tsing-Hua University, Hsin-Chu, Taiwan

<sup>2</sup> Department of Applied Mathematics,

National Hsinchu University of Education, Hsin-Chu, Taiwan

Received \_\_\_\_\_; accepted \_\_\_\_\_

## ABSTRACT

We study the migration and resonant capture of planetesimals in a planetary system consisting of a gaseous disc analogous to the primordial solar nebula and a Neptune-like planet. Using a simple treatment of the drag force we find that planetesimals are mainly trapped in the 3:2 and 2:1 resonances and that the resonant populations are correlated with the gaseous drag strength in a sense that the 3:2 resonant population increases with the stronger gaseous drag, but the 2:1 resonant population does not. Since planetesimals can lead to the formation of larger bodies similar to asteroids and Kuiper Belt Objects, the gaseous drag can play an important role in the configuration of a planetary system.

*Subject headings:* circumstellar matter – planetary systems – stellar dynamics

## 1. Introduction

The discovery of more than 160 planets orbiting other stars, extra-solar planets, opened a window of astronomy, which could eventually provide insight to understanding the fundamental questions about our own Solar System. Most of these extra-solar planets (exoplanets) were detected by the measurements of stellar radial velocities of their host star via the Doppler effect and several more recent detected exoplanets were discovered through the transit events. For example, the OGLE project has detected 5 transit exoplanets (Konacki et al. 2003, Bouchy et al. 2005), and the TrES team (using 10 cm telescopes) has discovered one transit planet (Alonso et al. 2004). All of the above 6 exoplanets were later confirmed by spectroscopic follow-up. Future observations using both methods will lead to the discoveries of additional systems, thereby improving the statistical significance of the population.

Among the many interesting properties exhibited by these planetary systems are the large range of masses, orbital periods and orbital eccentricities (Jiang et al. 2006). In particular, the relations between the orbital periods of different planets have been noted and are usually connected with the mean motion resonances. As an example of extra-solar multiple planetary systems which show the resonances, Ji et al. (2003) confirmed that the 55 Cancri planetary system is indeed in the 3:1 mean motion resonance by both the numerical simulations and secular theory. The GJ 876 and HD 82943 planetary systems are probably in 2:1 resonance as studied by Laughlin & Chambers (2001), Kinoshita & Nakai (2001), Gozdziewski & Maciejewski (2001) and also Ji et al. (2002). Moreover, the periods of small bodies in the Solar System such as asteroids and Kuiper Belt Objects (KBOs) are also seen to have similar connections with resonances. Thus, such types of dynamics may also play a role in the configuration of KBOs.

On the other hand, it has been shown that discs can affect the orbital evolution of

test particles within planetary systems (Jiang & Yeh 2004a, 2004b; Yeh & Jiang 2005). In particular, Jiang & Yeh (2004c) proposed a possible model of resonant capture for proto-KBOs driven by the gaseous drag, finding that many test particles can be captured into the 3:2 resonance, consistent with the observational results (Luu & Jewitt 2002).

To ensure that the gaseous drag influences the dynamics of planetesimals, sufficient gas must be present (about  $0.01M_{\odot}$  as suggested in Nagasawa et al. 2000) when the planetesimals are already formed. It is likely that molecular gas is present around the nearby star epsilon Eridani as found by Greaves et al. (1998), however, only an upper limit of 0.4 Earth masses in molecular gas is inferred from CO observations. This is to be compared to the primordial solar nebula where the minimum-mass solar nebula is about  $0.026 M_{\odot}$ .

Although there is evidence for a small amount of gas present in planetary systems, there may have been much more gas in the past. The km-sized planetesimals representing proto-asteroids were formed and likely influenced by the gaseous drag. During the above process, the gaseous component is gradually depleted from a more massive primordial nebula to the current limited molecular gas.

Whether the above scenario is viable would be related to the formation time-scale of km-sized planetesimals and the depletion time-scale of the gaseous discs. Cuzzi et al. (1993) argued that 10-100 km sized objects can be formed in about  $10^6$  years. Furthermore, observations by Kenyon & Hartmann (1995), Haisch et al. (2001) show that at the age of about  $10^6$  years, most low-mass stars are surrounded by the optically thick discs. However, by the age of  $10^7$  years, no such discs are detected. It is therefore possible that there is a phase in the evolution of the system where planetesimals are already formed while the gaseous disc is not yet depleted. We investigate this phase to examine the effect of gaseous drag for the planetesimal dynamics in this paper.

Since the km-sized planetesimals will grow into asteroids, KBOs or even planets, their distribution and orbital evolution are extremely important for understanding the history of planetary systems. Based on a disc model analogous to the primordial solar nebula, we study the resonant capture of planetesimals under the influence of a gaseous disc for a given planetary system. In particular, we study the possibility for correlations between the gaseous drag strength and the resonant populations and examine the possible parameter space for which the drag-induced resonant capture could explain the resonant populations of a planetary system.

We present our model and assumptions in § 2. § 3 describes the evolution of planetesimals and the stability tests. Finally, we discuss the results and conclude in the last section.

## 2. The Model

We consider the motion of a test particle influenced by the gravitational force from the central star, a planet and the proto-stellar disc. This disc, which is mainly composed of gas, exerts a drag on the planet and the test particles. These test particles are envisioned to represent planetesimals such as proto-asteroids and proto-KBOs. We assume that the mass of central star  $\mu_1 = 1M_\odot$ , and the planet's mass is taken to be similar to the Neptune's mass, i.e.  $\mu_2 = 5 \times 10^{-5}M_\odot$ . We assume the test particle represents a planetesimal with a radius about 10 km, with a mass assumed to be about  $\mu_3 = 4.3 \times 10^{-15}M_\odot$  (when the density is similar with the Pluto's). The coordinates of the central star, the planet and the planetesimal are  $(0, 0)$ ,  $(x, y)$  and  $(\xi, \eta)$ , respectively.

In this paper, we consider the general situation that the planet is free to move on any non-circular orbit.

## 2.1. The Units

In this paper, the unit of mass is  $M_\odot$  and the unit of length is 30 AU. Since we set the gravitational constant  $G = 1$ , the total simulation time,  $3.8 \times 10^5$ , which would correspond to  $10^7$  years. All simulations start from  $t = 0$  and terminate at  $t = t_{\text{end}} = 123200\pi \sim 3.8 \times 10^5$ .

## 2.2. The Equations of Motion

In this paper, we only consider the coplanar case, so all motions are in a two dimensional plane. The equations of motion are

$$\left\{ \begin{array}{l} \frac{d^2 x}{dt^2} = -\mu_1 \frac{x}{r^3} - \frac{\alpha}{\mu_2} \left( \frac{dx}{dt} - v_x \right) \rho_N - \frac{dV_N}{dr} \frac{x}{r}, \\ \frac{d^2 y}{dt^2} = -\mu_1 \frac{y}{r^3} - \frac{\alpha}{\mu_2} \left( \frac{dy}{dt} - v_y \right) \rho_N - \frac{dV_N}{dr} \frac{y}{r}, \\ \frac{d^2 \xi}{dt^2} = -\mu_1 \frac{\xi}{r_1^3} + \mu_2 \frac{x-\xi}{r_2^3} - \frac{\alpha}{\mu_3} \left( \frac{d\xi}{dt} - v_\xi \right) \rho_T - \frac{dV_T}{dr_1} \frac{\xi}{r_1}, \\ \frac{d^2 \eta}{dt^2} = -\mu_1 \frac{\eta}{r_1^3} + \mu_2 \frac{y-\eta}{r_2^3} - \frac{\alpha}{\mu_3} \left( \frac{d\eta}{dt} - v_\eta \right) \rho_T - \frac{dV_T}{dr_1} \frac{\eta}{r_1}, \end{array} \right. \quad (1)$$

where

$$r^2 = x^2 + y^2, \quad (2)$$

$$r_1^2 = \xi^2 + \eta^2, \quad (3)$$

$$r_2^2 = (x - \xi)^2 + (y - \eta)^2. \quad (4)$$

The equations of motion in terms of  $x$  and  $y$  describe the planet's orbit and the equations of  $\xi$  and  $\eta$  give the orbit of a test particle. In Eq. (1),  $V_N$  is the disc potential for the planet. In other words, we define that  $V_N = V(r)$  to be the disc potential at the planet's location  $(x, y)$  where  $r$  is given by Eq. (2) and  $\rho_N = \rho(r)$  is the disc density at the planet's location. Similarly,  $V_T = V(r_1)$  is the disc potential at the test particle's location  $(\xi, \eta)$  where  $r_1$  is given in Eq. (3) and  $\rho_T = \rho(r_1)$  is the disc density at the location of the test particle.

The disc is represented by an annulus with inner edge  $r_i$  and outer edge  $r_o$ , where  $r_i$  and  $r_o$  are assumed to be constants. We choose  $r_i = 1/5$ ,  $r_o = 5/3$  in this paper. Since we

set the unit of length to be 30 AU,  $r_i$  corresponds to the location where the Jupiter was formed approximately and  $r_o$  corresponds to the outer edge of the Kuiper Belt. Thus, our choice of inner and outer edges of the gaseous disc is based on the possible properties of the proto-solar nebula.

The density profile of the disc is taken to be of the form  $\rho(r) = c/r^p$ , where  $r$  is the radial coordinate as in Eq. (2),  $c$  is a constant completely determined by the total mass of the disc and  $p$  is a natural number. In this paper, we set  $p = 2$  based on the theoretical work by Lizano & Shu (1989). This assumption is consistent with one of the models of the Vega debris disc (Su et al. 2005). Hence, the total mass of the disc is

$$M_d = \int_0^{2\pi} \int_{r_i}^{r_o} \rho(r') r' dr' d\phi = 2\pi c (\ln r_o - \ln r_i). \quad (5)$$

In this paper, the disc mass is assumed to be  $M_d = 0.01$ , which is the same order as the minimum-mass solar nebula ( $0.026 M_\odot$ ). It is also consistent with the observations by Beckwith et al. (1990) in which the discs have masses ranging from 0.001 to  $1 M_\odot$ . The disc's gravitational potential and force can be calculated by elliptic integrals as in Jiang & Yeh (2004b).

In Eq. (1), the Keplerian velocity of the gaseous material in the  $\xi$  direction is  $v_\xi = -\sqrt{\frac{\mu_1}{r_1}} \sin \theta_T$  and in the  $\eta$  direction is  $v_\eta = \sqrt{\frac{\mu_1}{r_1}} \cos \theta_T$ , where  $\theta_T = \tan^{-1}(\eta/\xi)$ . Similarly,  $v_x = -\sqrt{\frac{\mu_1}{r}} \sin \theta_N$  and  $v_y = \sqrt{\frac{\mu_1}{r}} \cos \theta_N$ , where  $\theta_N = \tan^{-1}(y/x)$ .

### 2.3. The Drag

In this system, we include the effect of the drag force from the gaseous disc. There are various forms for the drag force that could be employed. For example, Murray (1994) considered a general drag force per unit mass of the form:

$$\mathbf{F} = k\mathbf{V}g, \quad (6)$$

where  $k < 0$ ,  $\mathbf{V}$  is the particle’s velocity in the inertial frame, and  $g$  is a scalar function of its position and velocity.

On the other hand, the aerodynamic friction force per unit mass is given by (Fitzpatrick 1970, Fridman & Gorkavyi 1999)

$$\mathbf{F} = \frac{1}{2m} C_D A \rho V_r^2, \quad (7)$$

where  $C_D$  is the drag coefficient,  $m$  and  $A$  are the particle’s mass and cross-section,  $\rho$  is the gaseous density, and  $V_r$  is the magnitude of particle’s velocity relative to the gas.

The Epstein drag force per unit mass has also been adopted (see Youdin & Shu 2002, Youdin & Chiang 2004) and is given by

$$\mathbf{F} = \frac{4\pi}{3m} \rho_g c_g v a^2, \quad (8)$$

where  $\rho_g$  is the mass density of gas and  $c_g$  is the gas sound speed. The particle’s mass and size are  $m$  and  $a$  respectively. The relative velocity between a particle and gas is  $v$ .

Our disc is mainly composed of gas and we wish to approximate the disc’s gaseous drag acting on the planetesimals and planets. Motivated by the above expressions for the drag, we employ a unified formula which we use for both planetesimals and the planet. Thus, we assume that the drag force per unit mass is:

$$\mathbf{F} = -\frac{\alpha\rho}{m} \mathbf{V}, \quad (9)$$

where  $\alpha$  is assumed to be a constant,  $\mathbf{V}$  is the particle’s velocity relative to the Keplerian motion of the gaseous disc, and  $\rho$  is the gas density.

Although our drag differs from the Epstein drag, we can see that  $\alpha$  plays the role of  $4\pi c_g a^2/3$  of Epstein drag. To obtain an estimate of the value of  $\alpha$ , we (i) use Eq.(2) of Youdin & Chiang (2004) to calculate  $c_g$ , (ii) use the radius of our planetesimal particle,

10 km, to be the value of  $a$ , and find that  $4\pi c_g a^2/3$  is about  $8 \times 10^{-16}$ . We, thus, define  $\alpha_E \equiv 8 \times 10^{-16}$ . Due to the simple treatment of the disc drag and the uncertainty in  $\alpha$ , we adopt 3 different values of  $\alpha$ :  $\alpha_E$ ,  $5\alpha_E$ , and  $25\alpha_E$ .

For the planet, the drag force in  $x$  direction is  $-(\alpha/\mu_2)(dx/dt - v_x)\rho_N$  and thus this term appears in the first equation of Eq. (1). Similarly, there is a term  $-(\alpha/\mu_2)(dy/dt - v_y)\rho_N$  appears in the second equation of Eq. (1).

For the planetesimals, the drag force in the  $\xi$  and  $\eta$  directions are  $-(\alpha/\mu_3)(d\xi/dt - v_\xi)\rho_T$  and  $-(\alpha/\mu_3)(d\eta/dt - v_\eta)\rho_T$  in the third and fourth equation of Eq. (1), respectively.

## 2.4. The Simulations

A number of planetesimals (300) are randomly distributed in a belt region  $1.1 \leq r \leq 1.8$  with a uniform number density, where  $r$  is the radial coordinate. Assuming that one planetesimal is located at  $(\xi, \eta)$ , then we set its initial velocity  $(v_{o\xi}, v_{o\eta})$  to be  $v_{o\xi} = -(\sqrt{1/r_1}) \sin \theta_T$  and  $v_{o\eta} = (\sqrt{1/r_1}) \cos \theta_T$ , where  $\theta_T = \tan^{-1}(\eta/\xi)$ . Thus, the planetesimals are initially in circular motion.

To study the outcome of different drag strengths, we adopt 3 different values of the drag coefficient in our simulations. That is,  $\alpha = \alpha_E$  in model A,  $\alpha = 5\alpha_E$  in model B and  $\alpha = 25\alpha_E$  in model C.

The planet is always located at  $(1, 0)$  initially, and was set in circular motion initially for models A, B, and C. However, in order to test the influence of the planet's orbital eccentricity, we also consider a model (D) in which the planet moves on an initial eccentric orbit of  $e = 0.3$  with drag coefficient chosen to be  $\alpha = 5\alpha_E$ .

To study the resonance captures, the orbital semi-major axis and eccentricity for all the

planetesimals and planet are calculated. To make it clear,  $x_*$ ,  $y_*$  represent the coordinates of any particle. From Murray & Dermott (1999), we have

$$\begin{aligned} r_*^2 &= x_*^2 + y_*^2, \\ v^2 &= \left(\frac{dx_*}{dt}\right)^2 + \left(\frac{dy_*}{dt}\right)^2. \end{aligned}$$

Let  $h^2 = (x_* \frac{dy_*}{dt} - y_* \frac{dx_*}{dt})^2$ , then semi-major axis  $a$  and eccentricity  $e$  are defined by

$$a = \left(\frac{2}{r_*} - \frac{v^2}{\mu_1}\right)^{-1}, \quad (10)$$

$$e = \sqrt{1 - \frac{h^2}{\mu_1 a}}. \quad (11)$$

Based on the formula in Murray & Dermott (1999) and Fitzpatrick (1970), the 2:1 resonant argument  $\phi_{2:1}$  and 3:2 resonance argument  $\phi_{3:2}$  are also calculated as

$$\phi_{3:2} = 3\lambda_t - 2\lambda_N - \omega_t, \quad (12)$$

$$\phi_{2:1} = 2\lambda_t - \lambda_N - \omega_t, \quad (13)$$

where  $\lambda_t$  is the mean longitude of a planetesimal's orbit,  $\lambda_N$  is the mean longitude of the planet's orbit and  $\omega_t$  is the longitude of pericentre of a planetesimal's orbit.

The number of particles in a particular resonance at time  $t_i$  is defined to be the total number of particles with the difference between the maximum and minimum resonance arguments less than  $180^\circ$  during  $t_{i-1} < t < t_i$ . We set  $t_0 = 0, t_i = t_{i-1} + 800\pi$ , where  $i = 1, 2, \dots, 154$ .

### 3. Numerical Results

#### 3.1. Evolution of Planetesimals

The evolution of planetesimals on the  $x - y$  plane in the simulation of model A is illustrated in Fig. 1. The panel labelled 0 in Fig. 1 shows the initial positions of all 300

planetesimals. Based on this representation, it is difficult to discern the change in the distribution until the 9th panel. However, specifically it can be seen in the histograms of particle number versus the radial distance reveal the variation more clearly (see Fig. 2). In the 2nd panel of Fig. 2, a gap starts to develop and this gap becomes deeper and wider in the following panels. Finally, the gap encompasses the range from 1.5 to 1.7 after the 8th panel. The gap can also be seen in panels 10 and 11 of Fig. 1 and separates the planetesimal distribution into two rings. The outer ring (from  $r = 1.7$  to  $r = 1.8$ ) is thinner than the inner one (from  $r = 1.1$  to  $r = 1.5$ ) as one can see from Fig. 1 and 2.

In Fig. 3, we plot the final planetesimal distribution of model A in the  $a - e$  plane on the left panel and also the color contour of it on the right panel. There is a population with nearly circular orbits from  $a = 1.7$  to  $a = 1.8$ . They are the main population of the outer ring of Fig. 1 and 2 as one can estimate the total number from the color bar. From both panels and also the color bar, we find that some planetesimals are associated with 2:1, 3:2, 7:5, 4:3, 5:4, 6:5 resonances and that there are more planetesimals in 3:2 (at  $a = 1.33$ ) than those in 2:1 resonance (at  $a = 1.6$ ). However, in order to confirm whether a given planetesimal is captured into a particular resonance, the particular resonance argument has to be calculated during the whole simulation. Because the influence of the first order resonance, 2:1 and 3:2, are much stronger than the others, we calculate the 2:1 and 3:2 resonance arguments, i.e.  $\phi_{2:1}$  and  $\phi_{3:2}$ . Fig. 3 also shows that there is a non-resonant population (from  $a = 1.4$  to  $a = 1.5$ ) with nearly circular orbits. This population, together with all the resonant population between 1.1 and 1.5, become the main population of the inner wider ring of Fig. 1 and 2. The orbital eccentricities of the 2:1 resonant population are larger and thus these planetesimals have wider range in semi-major axis. Although this wider range might cover both rings and also the gap of Fig. 1 and 2, the number of this population is small so that they do not change the distribution.

The evolution of planetesimals' distribution for model B is plotted in Fig. 4. The evolution proceeds more rapidly than in model A. This could be due to a larger drag force for this model. For example, in the 2nd panel, there is already a gap in the belt. The planetesimals continue to migrate inward and the gap becomes wider as shown in panels 3 and 4. In the 5th panel, the planetesimals are seen to distribute into two parts, i.e. an inner ellipse and an outer ring. The inner ellipse precesses slowly starting from panel 6 until the end of the simulation. This behaviour is confirmed in the histograms in Fig. 5 as the gap begins to form in panel 2. The inward migration is also evident as particle number increases between  $r = 1$  and  $r = 1.5$ .

It can be seen in Fig. 6 that some planetesimals associated with the 2:1 and 3:2 resonances cluster around  $a = 1.6$  and  $a = 1.33$ . All the planetesimals associated with the 3:2 resonance have almost exactly the same semi-major axes and, moreover, there is no other non-resonant planetesimals around  $a = 1.33$ , explaining why the inner ellipse is so thin in Fig. 4.

In model C, the largest drag force is considered. The planetesimals' inward migrations are so fast that there is already a gap in the 1st panel of Fig. 7. A clear inner ellipse is formed in panel 2 and it precesses slightly at the following panels. With that small precession, the whole distribution seems to be a steady state. The histograms of Fig. 8 also confirm the existence of the gap. We point out that there are no planetesimals in the 2:1 resonance for this model (see Fig. 9).

Although the planet's orbital eccentricity is taken to be zero initially, its eccentricity is about 0.02 during the simulations for models A, B, and C. In model D, the strength of the drag force is assumed to be moderate, i.e. the same as the one in model B, but the initial orbital eccentricity of the planet is 0.3. Due to the drag, the inward migrations are still significant and the gap immediately appears in the 1st and 2nd panel of Fig. 10. However,

planetesimals continue to migrate inward from panel 3 to 11 until they arrive at the inner edge of the disc. Finally, there is a small ring at the disc’s inner edge and the planetesimals at the outer regions are distributed randomly. Indeed, the histogram in Fig. 11 shows that most planetesimals are at the inner edge.

We summarize the results on the number of planetesimals captured into 3:2 and 2:1 resonances in Fig. 12. For model A, the solid curves show that there are about 50 planetesimals captured into 3:2 resonance and about 40 into 2:1 resonance. It is also shown in panel b that the number of the 2:1 resonant planetesimals approaches the maximum earlier than the one of 3:2. On the other hand, for model B, the dotted curve shows that there are about 140 planetesimals captured into the 3:2 resonance. It is much more than the one for model A. However, The panel b shows that the number of planetesimals captured into the 2:1 resonance in model B is the same as the one in model A. Moreover, since there are no planetesimals in the 2:1 resonance for model C, there is no dashed curve in panel b. For model D, the long dashed curves show that only a few planetesimals are captured into the 3:2 and 2:1 resonances. Therefore, the planet’s eccentric orbit significantly reduces the probabilities of resonant captures.

### 3.2. The Stability Tests

To determine the stability of the results by perturbations in the initial orbital eccentricity, disc mass, and location of the inner and outer disc edge, we have carried out a simulation consisting of 30 planetesimals with parameters identical to those adopted in model B. The limited number of planetesimals used here allows one to carry out many tests quickly. In this standard simulation, all 30 planetesimals migrate inward and are captured into the 3:2 resonance.

To check the stability of the orbital evolution to the initial orbital eccentricities of planetesimals, a simulation was performed in which all planetesimals have initial orbital eccentricities  $e = 0.01$  with all other settings remaining the same as the standard one. These 30 planetesimals migrate inward of which 27 are captured into the 3:2 resonance. Because the difference with the standard case is only 3 planetesimals, which is one order of magnitude less than the total number, 30, we conclude that the system is stable in terms of the initial orbital eccentricities of planetesimals. For the results in which 300 planetesimals are used, we are confident that the result would be similar if the planetesimals' initial orbital eccentricities were changed slightly.

To test the stability in terms of the disc mass, i.e. the value of  $M_d$ , we ran two simulations, one with  $M_d = 0.009$  and another one with  $M_d = 0.011$  while keep all other settings the same as the standard one. Note that  $M_d = 0.01$  in the standard case. For both simulations, all the 30 planetesimals migrate inward and are captured into the 3:2 resonance. Thus, the system is stable to perturbations in the disc mass.

To check the stability in terms of the location of the disc's edges, i.e. the value of  $r_i$  and  $r_o$ , 4 simulations were carried out with  $r_i = 1/5 - 0.01$ ,  $r_i = 1/5 + 0.01$ ,  $r_o = 5/3 - 0.01$ ,  $r_o = 5/3 + 0.01$ , while all other settings remaining the same as the standard case. All the 30 planetesimals migrate inward and are captured into the 3:2 resonance for all 4 simulations. Hence, the system is stable in terms of perturbations to the disc inner and outer edges.

#### 4. Discussions and Conclusions

In this paper, we have investigated the effect of different strengths of the gaseous drag on the resonant capture into the 3:2 and 2:1 resonances. For a small drag force as in model A, there are about 17 percent of planetesimals captured into the 3:2 resonance

and about 13 percent into the 2:1 resonance. For a moderate drag force as in model B, the fraction of planetesimals captured into 2:1 is still about 13 percent but the fraction for the 3:2 resonance increases to 47 percent. When a stronger drag force is used as in model C, the fraction of planetesimals captured into the 3:2 resonance greatly increases up to about 60 percent. In contrast, the number for the 2:1 resonance becomes zero. Therefore, the numerical results of the resonant capture process reveal that it is very sensitive to the strength of the gaseous drag. Since the planetesimals are captured into resonances during their inward migrations, the stronger drag increases the speed of inward migration, so, equivalently, the resonant population in capture processes is correlated with the speed of inward migration.

For a model in which the planet has an initially eccentric orbit, less than 3 percent of the planetesimals are trapped into the 3:2 and 2:1 resonances. Hence, the assumption of a large finite eccentricity nearly destroys the possibility of resonant captures.

To understand the difference between the 3:2 and 2:1 resonant captures, there are mainly two possibilities:

(1) the details of capture processes for the 3:2 and 2:1 resonances are fundamentally different, strongly depend on the migration speed of planetesimals.

(2) under our assumptions, there are more planetesimals passing the 3:2 resonant region during the simulations, so that more planetesimals are captured into the 3:2 resonance, even though the capture probabilities for 3:2 and 2:1 resonances are similar.

In order to understand whether the 2nd explanation is correct, we estimate the capture probability for both the 3:2 and 2:1 resonances. Let us assume that the potential candidates to be captured into the 2:1 resonance are those planetesimals initially located between the outer edge ( $r = 1.8$ ) and the 2:1 resonant region (about  $r = 1.6$ ). Since there are 300

planetesimals uniformly distributed in the region  $1.1 \leq r \leq 1.8$ , the potential number of planetesimals to be captured into the 2:1 resonance is

$$300 \times \frac{(1.8^2 - 1.6^2)}{(1.8^2 - 1.1^2)} \sim 100.$$

For model A, the total number of planetesimals captured into 2:1 is about 40, and the capture probability for the 2:1 resonance is about 40%.

The potential candidates to be captured into the 3:2 resonance, on the other hand, are those planetesimals initially located between the 2:1 resonant region (about  $r = 1.6$ ) and 3:2 resonant region (about  $r = 1.33$ ) plus those planetesimals initially located out of  $r = 1.6$  but *not* captured into the 2:1 resonance, so the potential number of planetesimals to be captured into the 3:2 resonance is

$$300 \times \frac{(1.6^2 - 1.33^2)}{(1.8^2 - 1.1^2)} + 60 \sim 177.$$

Thus, the capture probability for the 3:2 resonance is about  $50/177 = 28\%$ , which is smaller than the one for the 2:1 resonance.

For model B, the capture probability for the 2:1 resonance is still about 40%, however the total number of planetesimals captured into the 3:2 resonance increases significantly up to about 140. This could be due to the fact that some planetesimals initially located out of  $r = 1.6$  but *not* captured into the 2:1 resonance are also captured into the 3:2 resonance in time due to fast inward migrations.

Since the potential number of planetesimals to be captured into the 3:2 resonance is again 177, the capture probability for the 3:2 resonance is  $140/177$ , which is about 79%. Therefore, not only is the number of planetesimals passing into the 3:2 resonant region larger than the one for the 2:1 resonance, but also that the capture probability of the 3:2 resonance is larger than that of the 2:1 resonance.

For the largest gaseous drag considered (model C), the speed of inward migration is highest and even more planetesimals are in the 3:2 resonance. However, in this case, the number of particles in the 2:1 resonance vanishes.

From the above analysis for models A, B, and C, we confirm that the details of the 3:2 and 2:1 resonant capture are fundamentally different. As discussed in Peale (1976) and Murray & Dermott (1999), the resonant relations are determined by the influence of the planet on the planetesimals. In particular, during the conjunctions, the net tangential force experienced by the planetesimal is key because it can change the planetesimal’s angular momentum.

In the case when the planet moves on a circular orbit and the planetesimals are assumed to move on eccentric orbits, there is no net tangential force if the conjunctions occur exactly at the peri-center or apo-center. When the conjunctions occur at any other point on the orbit, the symmetry is destroyed, and thus, there is net tangential force. For a dense population of planetesimals moving on the same eccentric orbit, the net tangential force would cause about half of them to gain angular momentum and another half to lose angular momentum. If all these planetesimals were driven to migrate inwards due to the drag, (1) those which gain angular momentum would expand their orbits a bit and could be captured into the resonance, (2) those which lose angular momentum would continue to migrate inward. Since (a) the planetesimals might move on different orbits and (b) the exact locations of the repeated conjunctions are not known, it is difficult to estimate the capture probability.

The symmetry is further destroyed when the planet moves on the orbit with large eccentricity 0.3. As a result, it is more difficult for those conjunctions which lead to planetesimals gaining angular momentum to take place repeatedly. Thus, there are few planetesimals captured into the resonances in model D.

For the Kuiper Belt in the outer Solar System, objects are known to occupy the 3:2 and 2:1 resonant regions. The conventional mechanism explaining these resonances relies on the resonant capture by an outwardly migrating Neptune with a migration time-scale  $\tau = 2 \times 10^6$  years (Malhotra 1995). This migration was assumed to start in the late stages of the genesis of the Solar System when the formation of the gas giant planet was largely complete, the solar nebula had lost its gaseous component, and the evolution was dominated by the gravitational interactions. However, this mechanism is based on an assumption of pure radial orbital migrations. The generality of this mechanism is unclear if a more realistic orbit of Neptune were chosen. As shown by the numerical simulations in Thommes et al. (1999) and the analytic calculations in Yeh & Jiang (2001), Neptune’s orbital eccentricity shall not be zero during the outward migration. Because Neptune is currently moving on a circular orbit, a massive disc is needed to circularize Neptune’s orbit if the outward migration did happen.

On the other hand, our results show that the drag-induced resonant capture can explain the existence of objects in both 3:2 and 2:1 resonances, but the ratio of these two populations will depend on the gaseous drag strength. The similarity between the conventional picture and our mechanism reflects the fact that both captures are due to the relative motions between the planet and the small bodies. The main difference is the causes of the relative motions.

Finally, our results (model D) also show that the resonant capture occurs provided that the planet’s orbital eccentricity is not too large. This result could place some constraint on the possible orbital history of the planet. For example, from this point of view, in the conventional picture, Neptune will be able to capture the KBOs into the resonances only when its eccentricity is reduced to be smaller than 0.3. This further constrains the orbital history and the timing of Neptune’s migration if it did significantly contribute on the

resonant capture of 3:2 and 2:1 resonant KBOs.

### **Acknowledgment**

We acknowledge the anonymous referee's many good suggestions. We especially thank Prof. R. Taam for his efforts in improving the presentation. We are grateful to the National Center for High-performance Computing for computer time and facilities.

This work is supported in part by the National Science Council, Taiwan, under Ing-Guey Jiang's Grants: NSC 94-2112-M-008-010 and also Li-Chin Yeh's Grants: NSC 94-2115-M-134-002.

## REFERENCES

- Alonso, R., Brown, T. M., Torres, G., Latham, D. W., Sozzetti, A., Mandushev, G., Belmonte, J. A., Charbonneau, D., Deeg, H. J., Dunham, E. W., O'Donovan, F. T., Stefanik, R. P. 2004, *ApJ*, 613, L153
- Beckwith, S. V. W., Sargent, A. I., Chini, R. S., Guesten, R. 1990, *AJ*, 99, 924
- Bouchy, F., Udry, S., Mayor, M., Moutou, C., Pont, F., Iribarne, N., da Silva, R., Ilovaisky, S., Queloz, D., Santos, N., Segransan, D., Zucker, S. 2005, *A&A*, submitted, astro-ph/0510119
- Cuzzi, J. N., Dobrovolskis, A. R., Champney, J. M. 1993, *Icarus*, 106, 102
- Fitzpatrick, P. M. 1970, *Principles of Celestial Mechanics*, (New York: Academic Press)
- Fridman, A. M., Gorkavyi, N. N. 1999, *Physics of Planetary Rings*, (Berlin, Heidelberg: Springer-Verlag)
- Gozdziewski, K., Maciejewski, A. J. 2001, *ApJ*, 563, L81
- Greaves, J. S., Holland, W. S., Moriarty-Schieven, G., Jenness, T., Dent, W. R. F., Zuckerman, B., McCarthy, C., Webb, R. A., Butner, H. M., Gear, W. K., Walker, H. J. 1998, *ApJ*, 506, L133
- Haisch, K. E., Lada, E. A., Lada, C. J. 2001, *ApJ*, 553, L153
- Hatzes, A. P., Cochran, W. D., McArthur, B., Baliunas, S. L., Walker, G. A. H., Campbell, B., Irwin, A. W., Yang, S., Kurster, M., Endl, M., Els, S., Butler, R. P., Marcy, G. W. 2000, *ApJ*, 544, L145
- Ji, J., Kinoshita, H., Liu, L., Li, G. 2003, *ApJ*, 585, L139

Ji, J., Li, G., Liu, L. 2002, ApJ, 572, 1041

Jiang, I.-G., Yeh, L.-C. 2004a, AJ, 128, 923

Jiang, I.-G., Yeh, L.-C. 2004b, Int. J. Bifurcation and Chaos, 14, 3153

Jiang, I.-G., Yeh, L.-C. 2004c, MNRAS, 355, L29

Jiang, I.-G., Yeh, L.-C., Hung, W.-L., Yang, M.-S. 2006, MNRAS, 370, 1379

Kenyon, S. J., Hartmann, L. 1995, ApJS, 101, 117

Kinoshita, H., Nakai, H. 2001, PASJ, 53, L25

Konacki, M., Torres, G., Jha, S., Sasselov, D. D. 2003, Nature, 421, 507

Laughlin, G., Chambers, J. 2001, ApJ, 551, L109

Lizano, S., Shu, F. H. 1989, ApJ, 342, 834

Luu, J. X., Jewitt, D. C. 2002, ARAA, 40, 63

Malhotra, R. 1995, AJ, 110, 420

Murray, C. D. 1994, Icarus, 112, 465

Murray, C. D. & Dermott, S. F. 1999, Solar System Dynamics, (Cambridge: Cambridge University Press)

Nagasawa, M., Tanaka, H., Ida, S. 2000, AJ, 119, 1480

Peale, S. J. 1976, Annual Review of Astronomy and Astrophysics, 14, 215

Su, K. Y. L. et al. 2005, ApJ, 628, 487

Thommes, E. W., Duncan, M. J., Levison, H. F. 1999, Nature, 402, 635

Yeh, L.-C., Jiang, I.-G. 2001, ApJ, 561, 364

Yeh, L.-C., Jiang, I.-G. 2005, Proceeding of the 9th Asian-Pacific Regional IAU Meeting  
(APRIM), in press

Youdin, A. N., Chiang, E. I. 2004, ApJ, 601, 1109

Youdin, A. N., Shu, F. H. 2002, ApJ, 580, 494

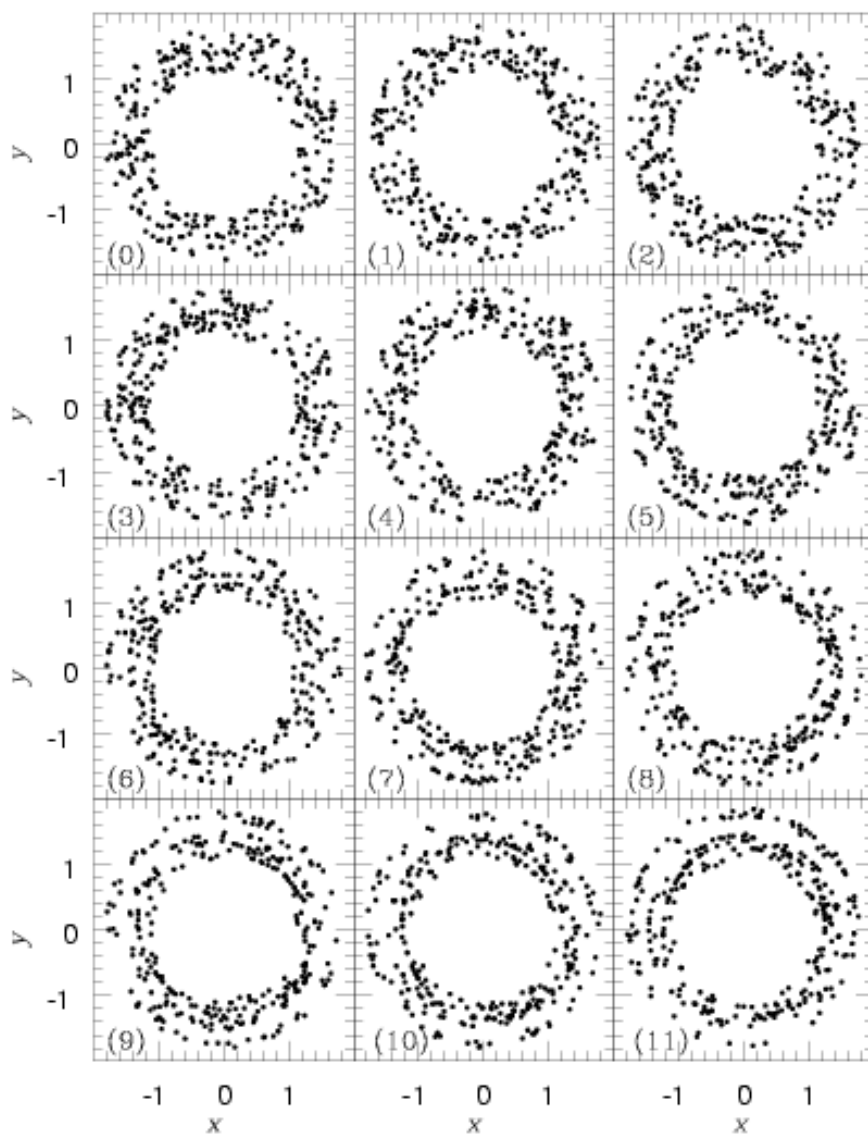


Fig. 1.— The model A: the evolution of particle distributions in the  $x - y$  plane. The time between successive panels corresponds to  $11200\pi$ .

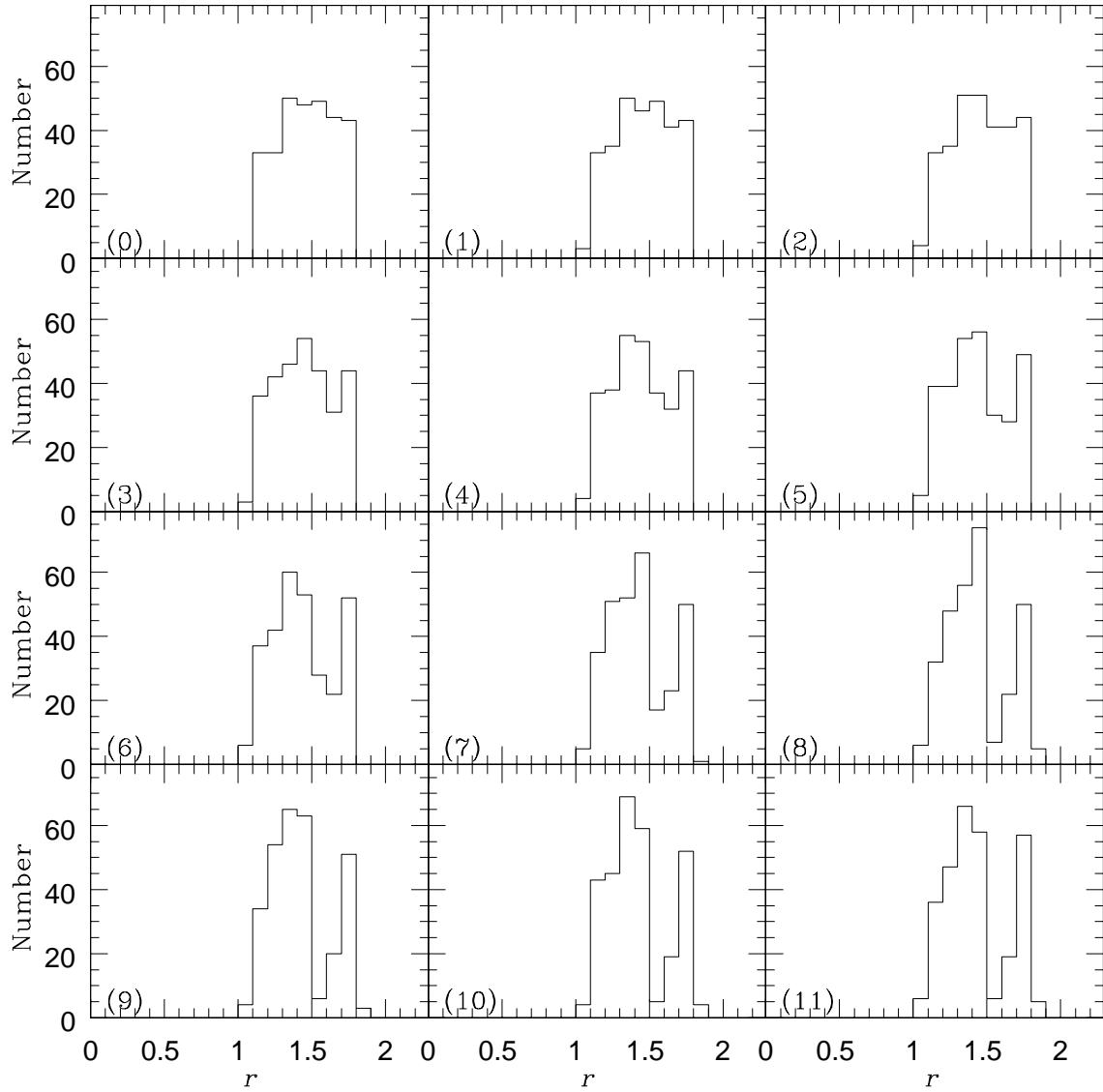


Fig. 2.— The model A: the histograms of particle distributions in the radial coordinate. The time between successive panels corresponds to  $11200\pi$ .

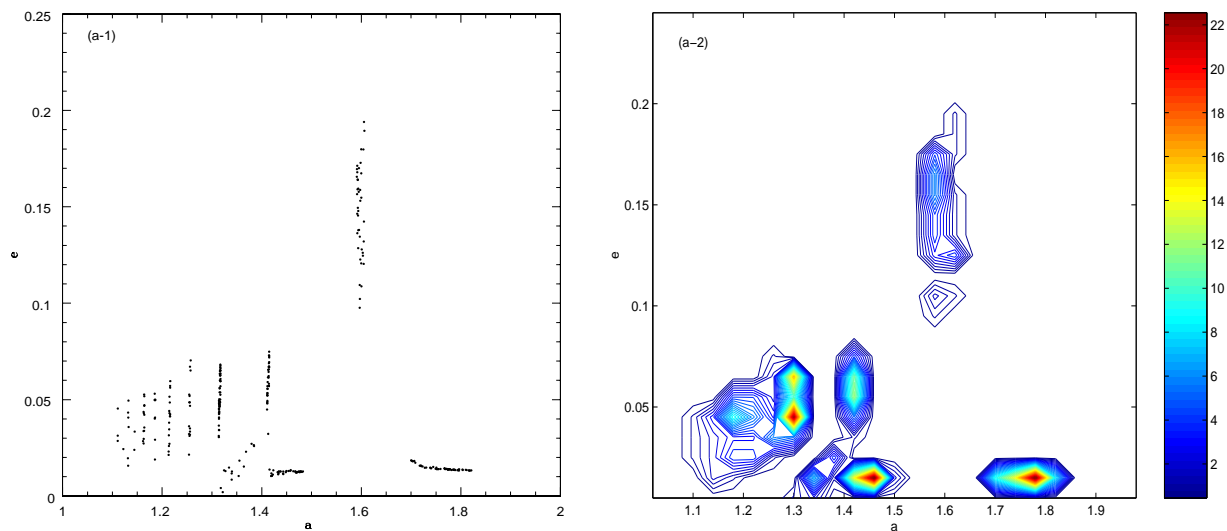


Fig. 3.— The model A: the particle distribution in the  $a$ - $e$  plane at the end of simulation, i.e.  $t = 123200\pi$ . The right color panel shows the number of particles at the particular area.

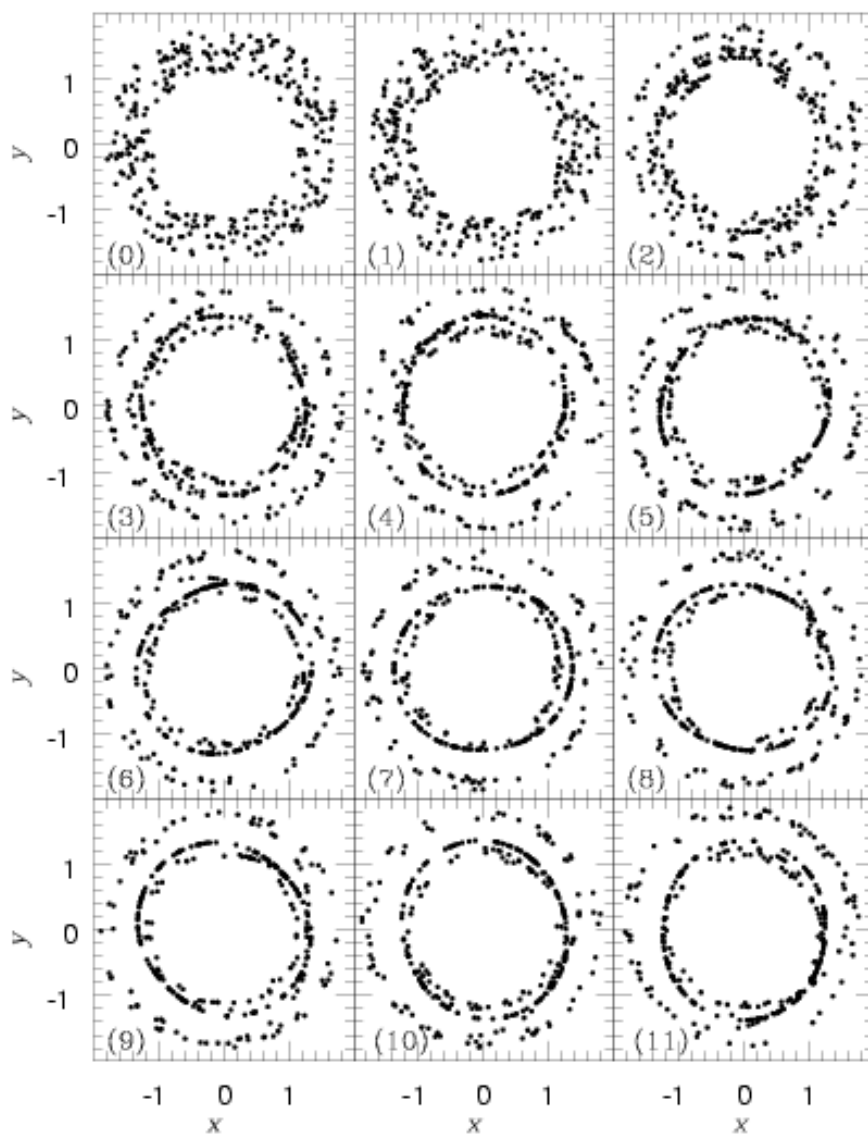


Fig. 4.— The model B: the evolution of particle distributions in the  $x - y$  plane. The time between successive panels corresponds to  $11200\pi$ .

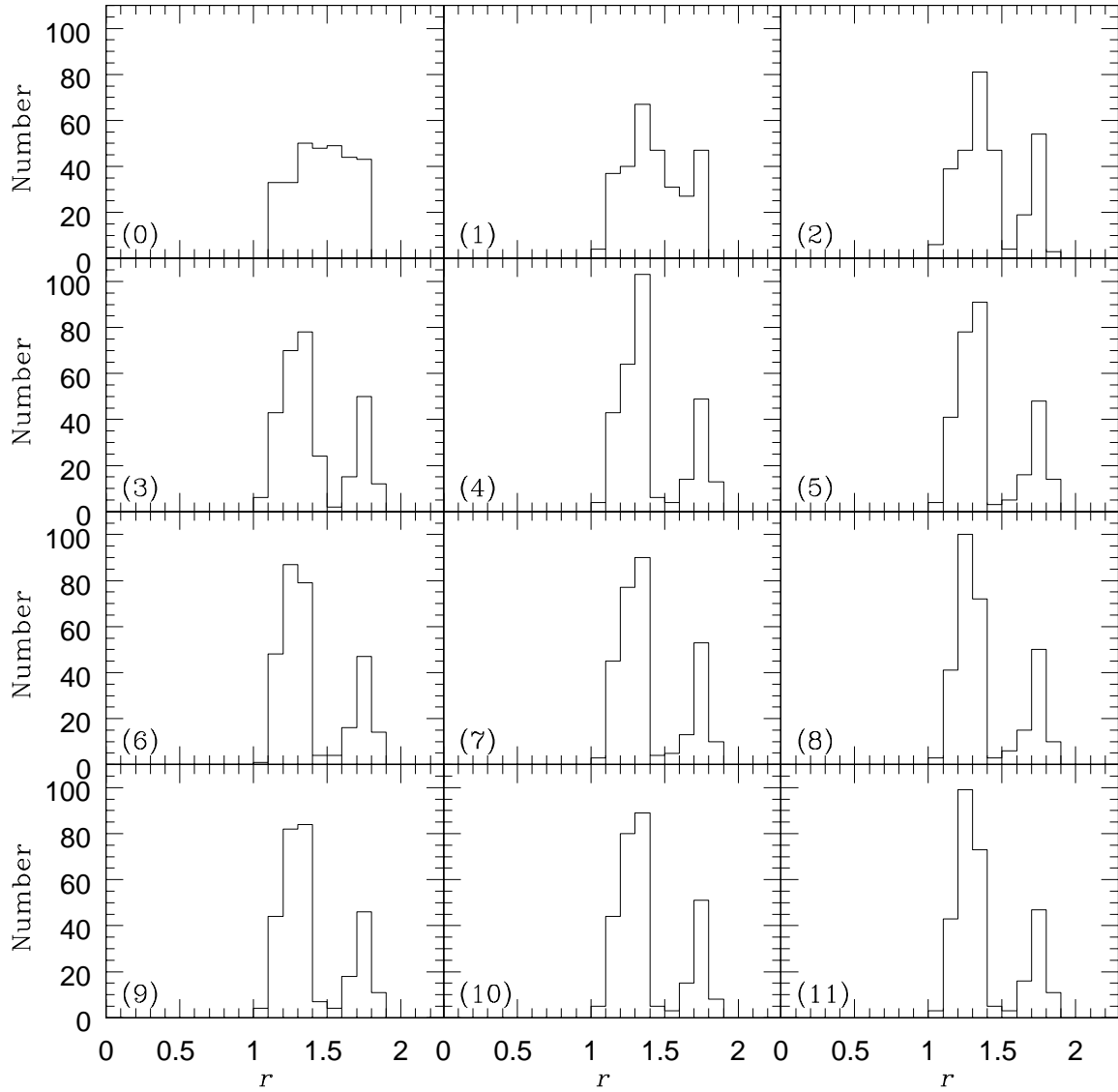


Fig. 5.— The model B: the histograms of particle distributions in the radial coordinate. The time between successive panels corresponds to  $11200\pi$ .

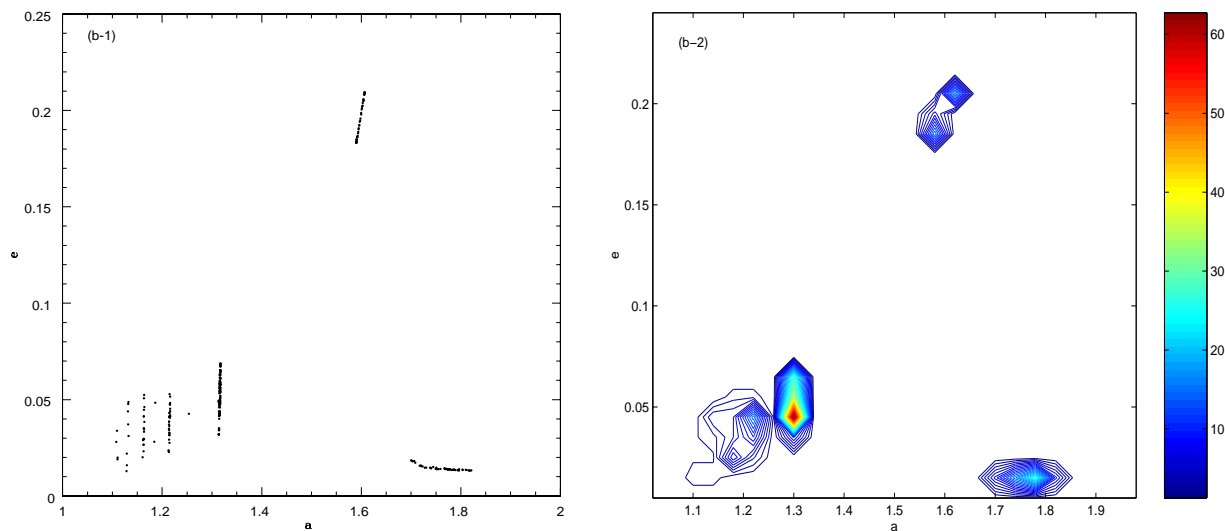


Fig. 6.— The model B: the particle distribution in the  $a$ - $e$  plane at the end of simulation, i.e.  $t = 123200\pi$ . The right color panel shows the number of particles at the particular area.

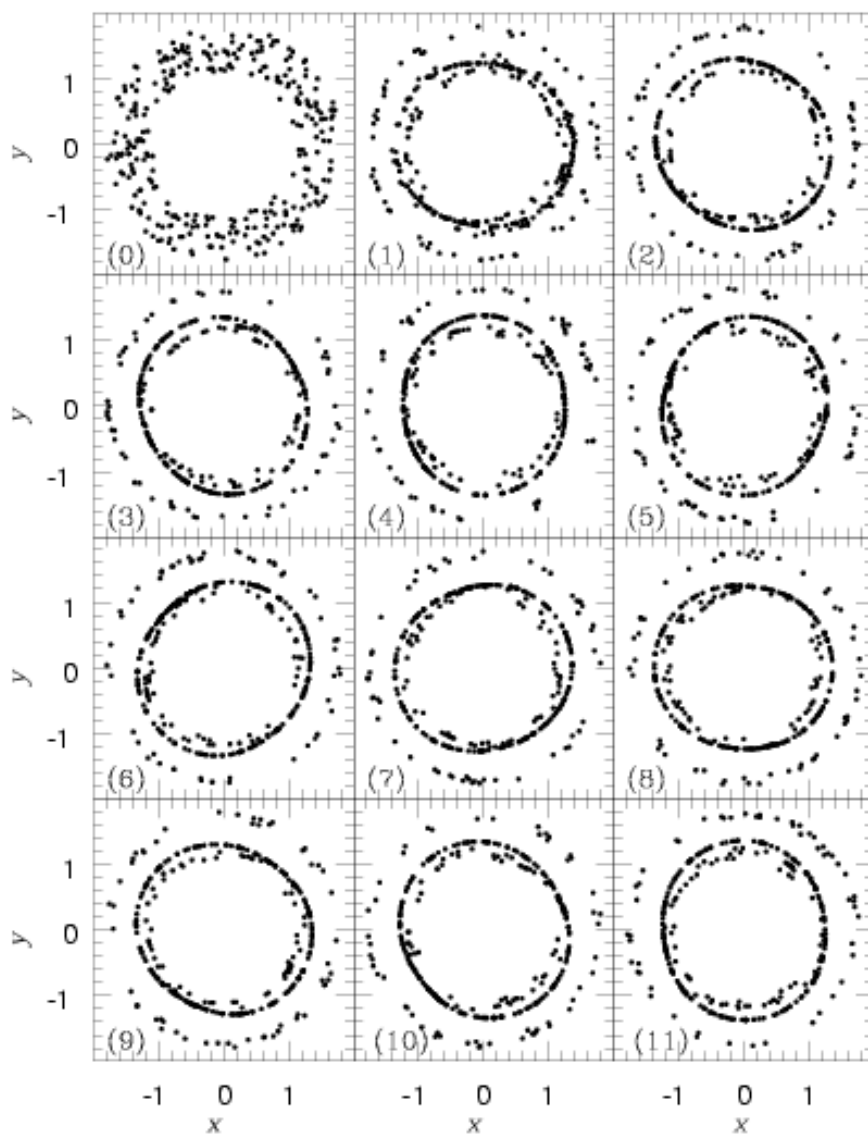


Fig. 7.— The model C: the evolution of particle distributions in the  $x - y$  plane. The time between successive panels corresponds to  $11200\pi$ .

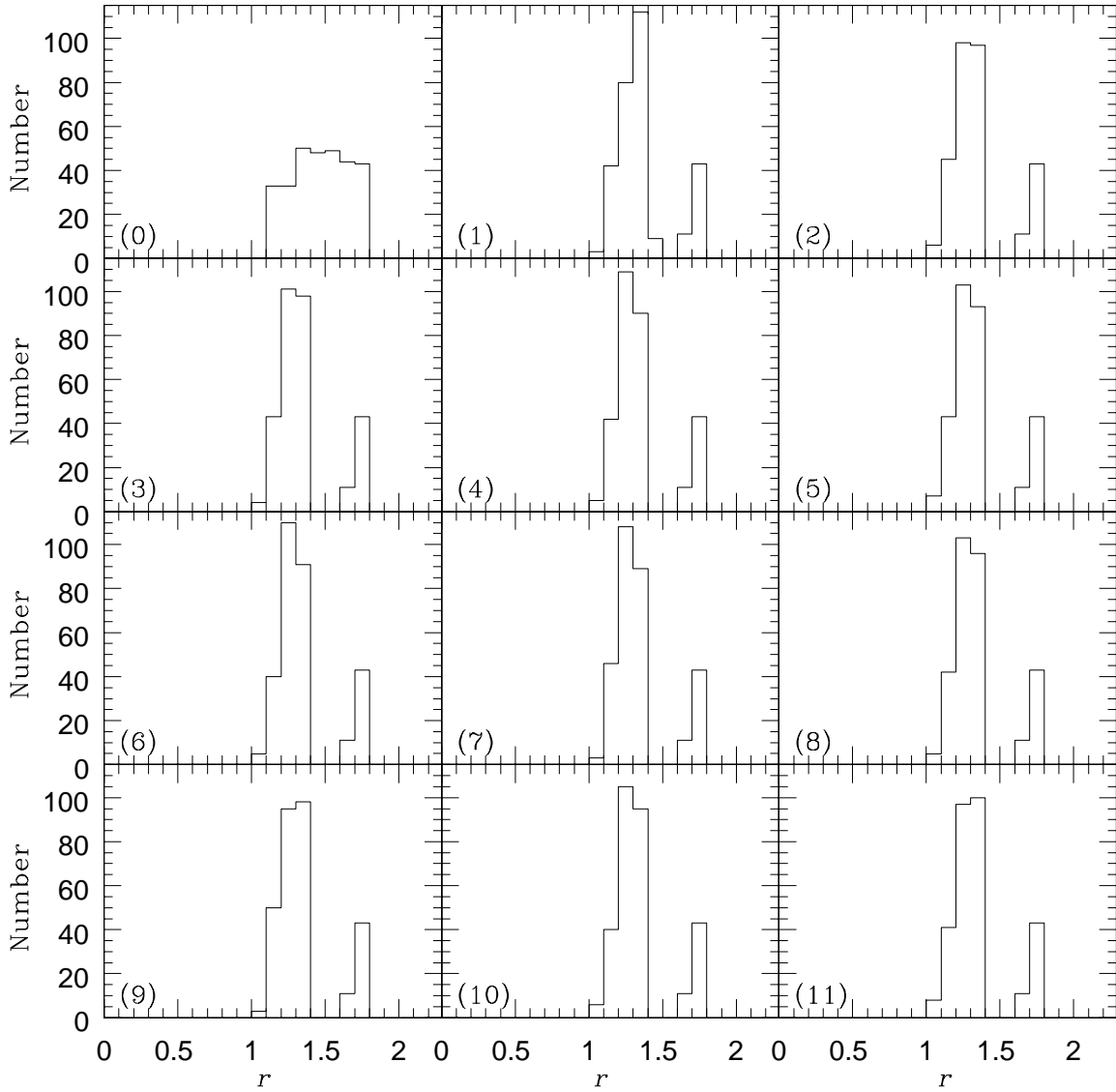


Fig. 8.— The model C: the histograms of particle distributions in the radial coordinate. The time between successive panels corresponds to  $11200\pi$ .

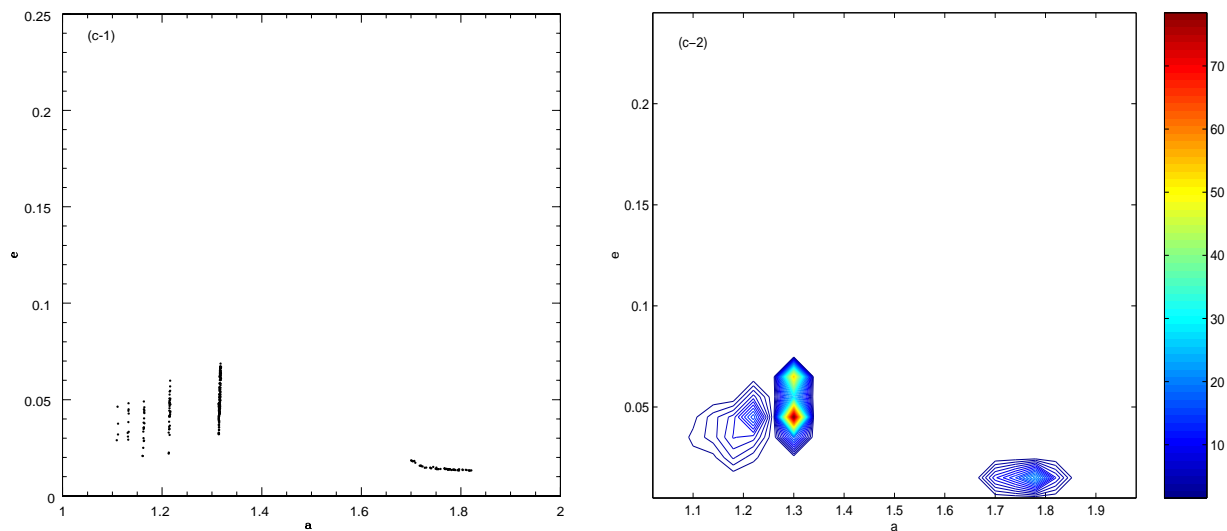


Fig. 9.— The model C: the particle distribution in the  $a$ - $e$  plane at the end of simulation, i.e.  $t = 123200\pi$ . The right color panel shows the number of particles at the particular area.

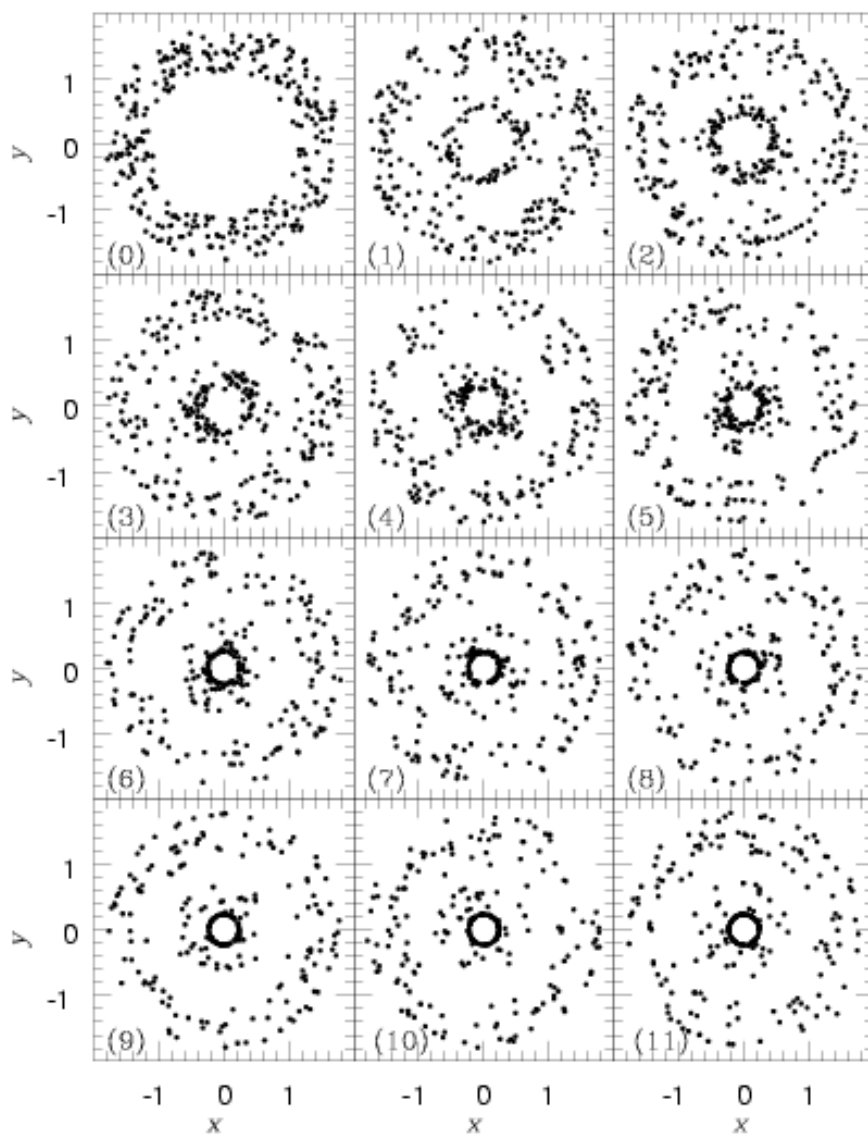


Fig. 10.— The model D: the evolution of particle distributions in the  $x - y$  plane. The time between successive panels corresponds to  $11200\pi$ .

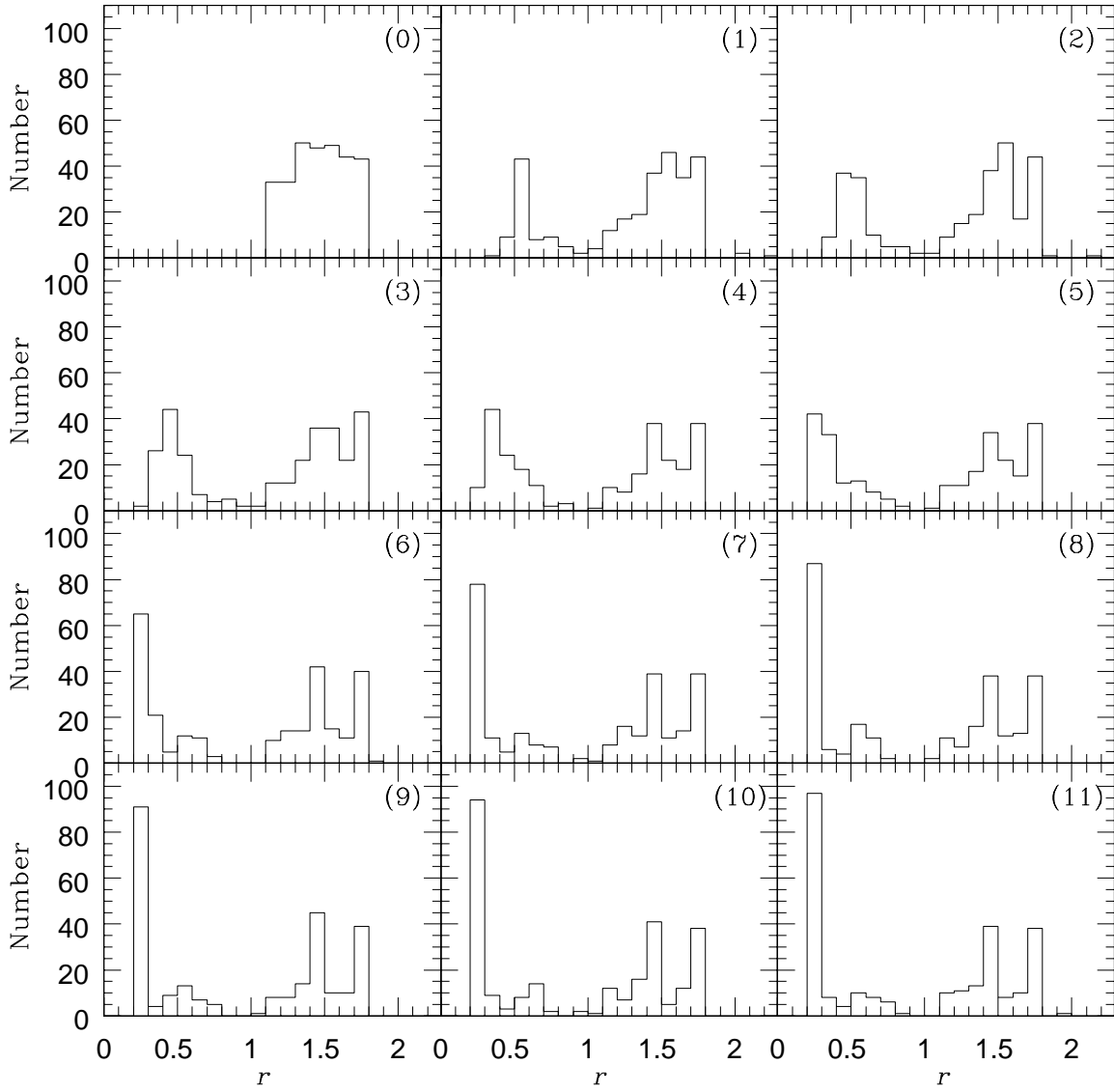


Fig. 11.— The model D: the histograms of particle distributions in the radial coordinate. The time between successive panels corresponds to  $11200\pi$ .

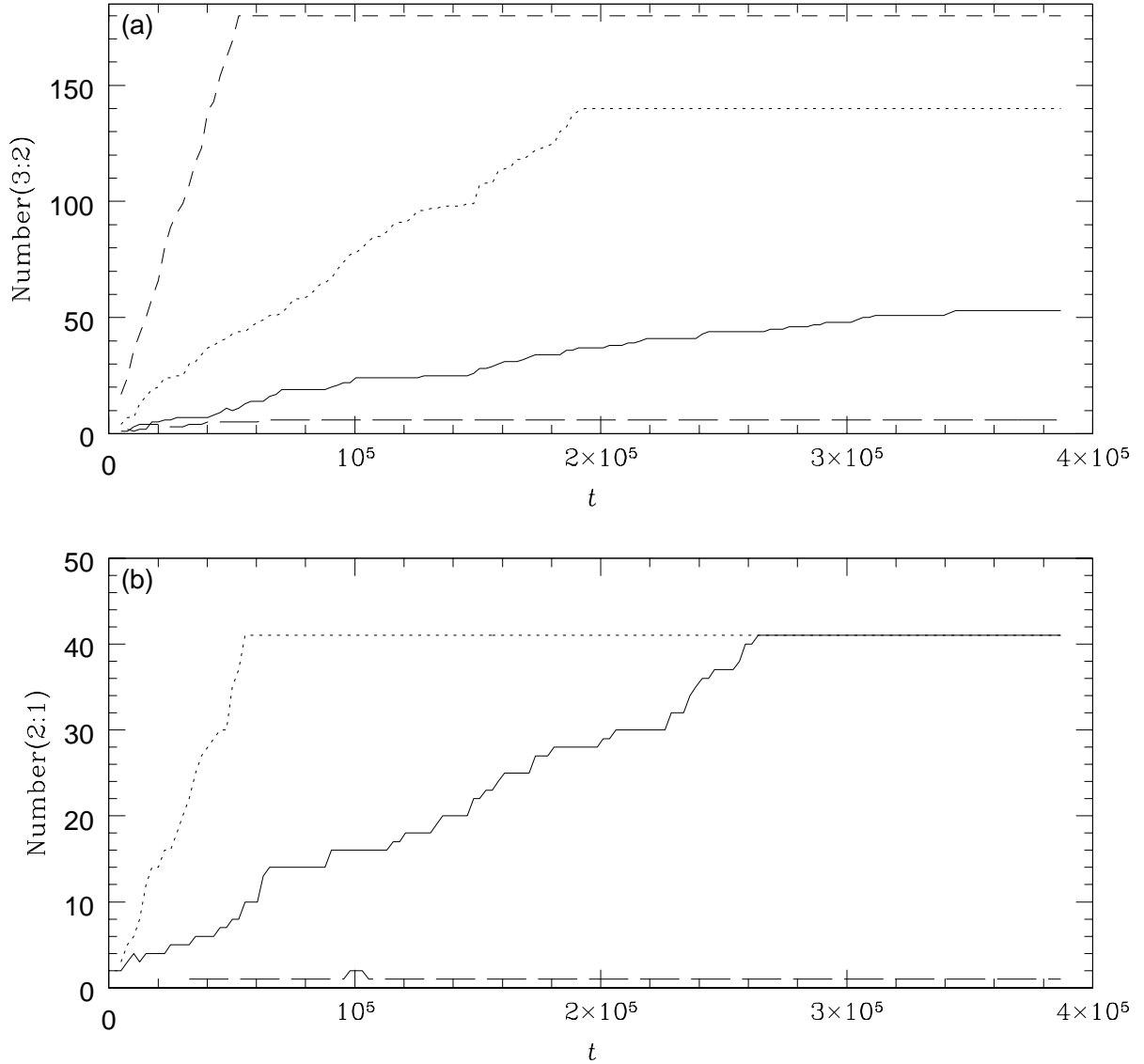


Fig. 12.— The number of resonant particles as a function of time. The panel (a) is for the 3:2 resonance and panel (b) is for the 2:1 resonance. The solid curves are for model A; the dotted curves are for model B; the dashed curve is for model C; the long dashed curves are for model D. Please note that there are only 3 curves in panel (b) because no particle in the 2:1 resonance in model C.